

# Ab-initio Kinetic Monte Carlo Model of Ionic Conduction in Bulk Yttria-stabilized Zirconia

Eunseok Lee, Friedrich B. Prinz, and Wei Cai

Department of Mechanical Engineering, Stanford University, Stanford, CA 94305

**Abstract.** We present a kinetic Monte Carlo (kMC) model to simulate the ionic conduction in bulk single crystal Yttria-stabilized Zirconia. An interacting energy barrier model is developed to take into account the interactions between ions by combining density functional theory calculations and the cluster expansion method. The electrical impedance as a function of doping concentration is predicted by kMC simulations. The optimal doping concentration and the effective energy barrier are predicted to be consistent with the experimental observations. We also compute the electrical impedance at different dopant distributions, which helps us to identify the mechanisms of the ionic conductivity enhancement by rearranging dopants and predict the optimal dopant distribution.

PACS numbers: 82.20.Wt, 66.30.-h, 82.47.Ed, 82.45.Gj

## 1. Introduction

Solid electrolyte is an important component in many applications, *e.g.* solid oxide fuel cell (SOFC) and oxygen sensor, and hence has been extensively studied. In particular, the necessity of reducing the operating temperature of SOFC without losing ionic conductivity encourages the development of new solid electrolyte materials with highly enhanced ionic conductivity. [1, 2] Recent progress by engineering the microstructure of solid electrolytes [3, 4, 5, 6, 7, 8, 9, 10, 11, 12, 13, 14, 15, 16] motivates another way to improve ionic conductivity by tailoring dopant distribution in existing electrolyte materials, which is made possible by atomic layer deposition.

Predicting the optimal dopant distribution requires a comprehensive understanding of the different mechanisms that control ionic conductivity, which has not been fully achieved so far. A major challenge originates from the fact that the unit steps of ionic conduction occurs in nano-meter length scale and pico-second time scale, at which experimental observations are very difficult. Atomistic simulations can potentially provide an alternative way to the experimental methods to study the mechanisms of ionic conduction.

Shimojo and Okazaki [17] used molecular dynamics to simulate the vacancy diffusion in Yttria-stabilized Zirconia (YSZ). They concluded that the difference of conductivity at different doping concentration is not caused by the interaction energy as a function of the distance between vacancy and Yttrium but instead originates from the increased energy barrier caused by Y ions on the path of vacancy jump. Meyer *et al.* [18] performed Monte Carlo simulations to study the conductivity of aliovalent doped fluorite oxides. They accounted for three different types of interactions between vacancy and dopant and concluded that the mobility of the vacancy is reduced when a dopant ion is located on the path of vacancy jump.

The use of density functional theory (DFT) calculations provided a way to calculate the energy barrier of vacancy jump accurately. [19, 20] Krishnamurthy *et al.* [21] computed three energy barriers of vacancy jump assuming that the energy barrier depends only on two cations on the path of vacancy jump and applied them to kinetic Monte Carlo (kMC) simulations of vacancy diffusion. Pornprasertsuk *et al.* [22, 23] computed 42 energy barriers considering six cations surrounding the jumping vacancy and used them in kMC simulation of vacancy diffusion. Both works showed that the conductivity changes with different doping concentration and predicted an optimal doping concentration corresponding to the maximum conductivity. Pornprasertsuk *et al.* [24] also calculated the electrical impedance of YSZ using kMC model, where the energy barriers are calibrated with the applied voltage and the internal voltage due to the ionic configuration.

Recently, the interaction between vacancies has received much attention. Pietrucci *et al.* [25] used molecular dynamics (MD) to investigate the contribution of vacancy-vacancy interaction to the ionic conductivity of YSZ. They observed a strong dependence of the activation energy barrier of vacancy jump on the position of other vacancies as

well as on the position of Y ions. The importance of the effect of vacancy-vacancy interaction to conductivity was also proposed in a kMC model for Praseodymium Doped Ceria developed by P.P. Dholabhai et al. [26]

The cluster expansion method has been used to fit to DFT data and to predict the ordering of ionic structure and diffusion coefficient of solid electrolyte. [27, 28, 29, 30] Van der Ven *et al.* [27] introduced the kinetically resolved activation (KRA) barrier model which accounts for energy difference before and after the jump of charge carrier. They applied these methods to the kMC simulations of the lithium diffusion in  $\text{Li}_x\text{CoO}_2$ . Predith *et al.* [30] used the cluster expansion method (CEM) to predict the global ground state of YSZ. Even though the main focus of their work is not ionic conductivity, these methods can be used to predict the energy of ionic configurations in the kMC simulation of ionic conductivity.

In our recent publication, we developed an interacting energy barrier model by combining the DFT and the CEM to account for the effect of ionic interactions on the energy barrier. [31] The coefficients in the cluster expansion method were fitted to a large set of DFT calculations performed with much larger supercells compared with those in previous works. KMC simulations were performed to study the effects of doping concentration and the dopant distribution on the ionic conductivity, from which we formulated two design principles of tailoring the dopant distribution to enhance the ionic conductivity. The optimal dopant distribution to enhance the ionic conductivity was predicted to be a superlattice.

The purpose of this paper is to describe our numerical method in sufficient detail, to support our previous findings with calculations of the electrical impedance, and to provide in-depth discussions on the physics of the predictions. The remaining of the paper is organized as follows. Section II describes the computational model used in this paper. The kMC model is described, and the interacting energy barrier model and cluster expansion method are explained. In section III, the developed computational model is applied to the simulation of vacancies in YSZ to study the effect of doping concentration on the ionic conductivity. Section IV presents the simulation results on the effect of dopant distribution on the ionic conductivity and the prediction of the optimal dopant distribution.

## 2. Computational Model

### 2.1. Kinetic Monte Carlo Model

The kinetic Monte Carlo (kMC) method is a variant of the Monte Carlo method and can simulate kinetic processes because time is also updated during the simulation. [32] YSZ maintains the cubic phase at intermediate temperature when the doping concentration is over 6 mol%. [59] The unitcell of cubic YSZ is shown in the Fig. 1. Each unitcell contains 4 sites to be occupied by cations ( $\text{Zr}^{4+}$  or  $\text{Y}^{3+}$ ), and 8 sites to be occupied by oxygen anions or vacancies. The cations occupy the cubic corners and the face-centers,

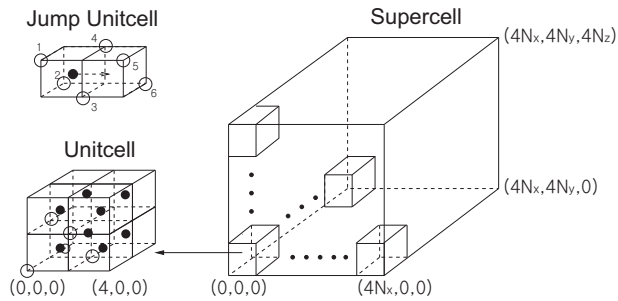


**Figure 1.** Simulation system of ionic diffusion in cubic YSZ using a supercell of dimension  $N_x[100] \times N_y[010] \times N_z[001]$ .  $\circ$ : Cation sites,  $\bullet$ : Anion sites.

and the oxygen anions and vacancies occupy the center of the 8 sub-cubes inside the unit cell. Therefore, the anion sites form a simple cubic sublattice. The simulation supercell is subjected to periodic boundary conditions (PBC) in all three directions and consists of  $N_x \times N_y \times N_z$  unitcells. For simplicity, all lengths are expressed in units of  $1/4$  of the lattice constant  $a_0$ . In this way, the coordinates of each cation and oxygen site can be specified by three integers. The coordinates of cations are even numbers and the coordinates for oxygen sites are odd numbers. The lattice constant is chosen to be  $5.14 \text{ \AA}$ , which corresponds to the experimental value for 8 mol% YSZ. [33]

Since the vacancy mechanism determines the ionic diffusion in YSZ, we simulate the oxygen vacancy diffusion instead of oxygen ion diffusion. Each oxygen vacancy can possibly jump to one of their six adjacent sites ( $\pm 2, \pm 2, \pm 2$ ) if the adjacent site is occupied by an oxygen anion. The jump unitcell is also shown in Fig. 1. For every vacancy, the probability rate  $j = \nu \exp(-E_b/k_B T)$  is calculated for every jump direction. Each possible jump is called an event.  $E_b$  is the free energy barrier of event and is calculated by the free energy difference between the current state and the transition state during the event.  $\nu$  is the jump trial frequency. ‡ Vacancy diffusion is simulated by selecting one event from all possible events and updating the vacancy positions and the physical time accordingly at each interaction. [32, 34]

## 2.2. Interacting Energy Barrier Model

Since selecting an event at each kMC step depends on the probability rate of each event, accurate calculation of the energy barrier of each event is essential for an accurate kMC simulation. Even though DFT calculation is usually accepted as a much more accurate method compared with empirical potential models, it is very challenging to calculate the energy barrier from DFT because of its heavy computational cost. Thus we need to develop an energy barrier model that is efficient but maintains an accuracy similar to DFT calculations.

Krishnamurthy *et al.* [21] developed an energy barrier model, in which the energy

‡ In this paper, we use the approximation  $\nu = 10^{13} s^{-1}$ , which is widely used for ceramic materials. [21, 23, 58]

barrier is determined by the chemical species of the two cations on the transition plane that the diffusing vacancy passes through (ions 3 and 4 in the jump unit cell in Fig. 1) and the energy barrier is increased as more Y ions occupy these two sites. This model predicts the optimal doping concentration (8-10 mol% at high temperature,  $T > 1000$  K) consistent with experimental observations. We will call this model the non-interacting model because the energy barriers for each vacancy jump and its reverse jump are the same, meaning that the system energy remains the same before and after each jump. However this is not true in ionic solids which have strong interactions between ions. Due to the ionic interactions, the energy is different before and after vacancy jump, unless the ionic configurations before and after vacancy jump are equivalent by symmetry. The ionic interaction makes the energy barrier of vacancy jump different in the forward and backward directions. Hence, to build a more physical energy barrier model, the ionic interactions must be considered.

The kinetically resolved activation (KRA) energy barrier model has been proposed for this purpose. [27, 28] In the KRA model, energy barrier is divided into a kinetic part and a thermodynamic part. The thermodynamic part is defined as the energy difference of system before and after the vacancy jump,  $\Delta E$ , and the kinetic part describes the energy barrier when  $\Delta E$  is zero,  $E_b^0$ . The kinetic part and the thermodynamic part are assumed to be independent each other in the KRA model. Thus the energy barrier  $E_b$  can be written as a function of  $E_b^0$  and  $\Delta E$ .

A simple linear function has been proposed to correct the energy barrier by a half of the energy difference after vacancy jump  $\Delta E$  [27, 28], *i.e.*  $E_b = E_b^0 + \Delta E/2$ . This function means that the saddle point remains the same (along the reaction coordinate) regardless of  $\Delta E$ . This is a good approximation only when  $\Delta E$  is much smaller than  $E_b^0$ . Since in our DFT calculations for YSZ,  $\Delta E$  is on the same order of magnitude as  $E_b^0$ , we designed a model applicable in the extended range of  $\Delta E$ .

The energy profile usually can be approximated by the summation of several sinusoidal functions. When  $\Delta E$  is zero, the energy profile during vacancy jump can be approximated by  $E(x) = E_b^0 \cos^2(\pi x)$ , where  $x$  is reaction coordinate; -0.5 indicates the state before vacancy jump and +0.5 indicates the state after vacancy jump. The energy barrier for the forward direction is the energy difference between  $x=0$  (saddle) and  $x=-0.5$  (local minimum). The energy barrier for the backward direction is the energy difference between  $x=0.5$  and  $x=0$ . If the energy changes after vacancy jump, we can assume that the energy profile is linearly shifted, *i.e.*  $E(x) = E_b^0 \cos^2(\pi x) + \Delta E x$ .

This changes the positions of the saddle point and local minimum as illustrated in Fig. 2(a). The energy barrier for the forward direction is obtained by finding a new local minimum and a new saddle point in the energy profile. If  $\Delta E$  is too large, the energy barrier predicted by this approach is less than zero. This means that there is no energy minimum before the vacancy jump. To avoid the negative energy barrier in the kMC simulations, the energy barriers less than 0.001 eV are all set to 0.001 eV. Once the energy barrier is obtained for the forward direction ( $E_b^{\text{FW}}$ ), the energy barrier for the backward direction ( $E_b^{\text{BW}}$ ) is set to  $E_b^{\text{FW}} - \Delta E$  to satisfy detailed balance. Using this

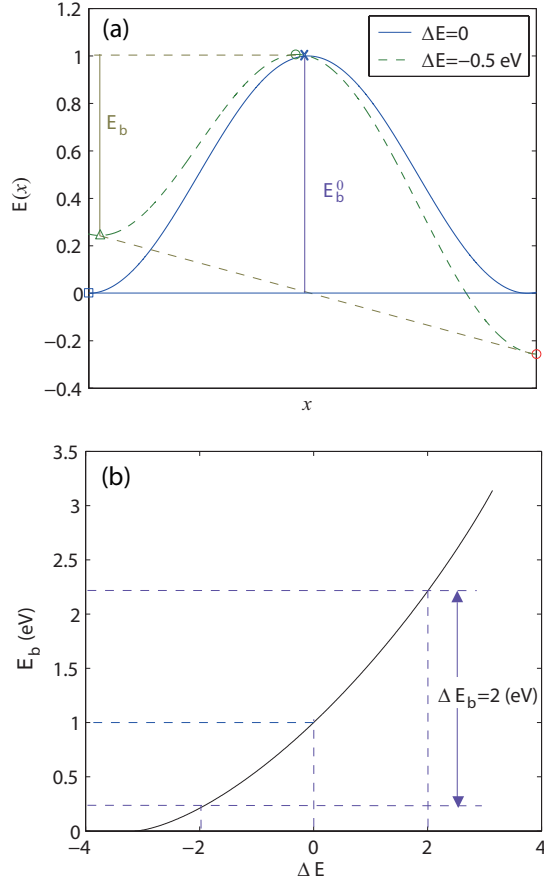


**Figure 2.** Interacting energy barrier model. (a) Energy profile for  $\Delta E = 0$  eV and  $\Delta E = -0.5$  eV. The saddle point changes from  $\times$  to  $\circ$  and the local minimum changes from  $\square$  to  $\triangle$  due to nonzero  $\Delta E$ . (b) Energy barrier as a function of  $\Delta E$ . For example, when  $\Delta E = -2$  eV,  $E_b^{\text{FW}} = 0.21$  eV and  $E_b^{\text{BW}} = 2.21$  eV.  $E_b^{\text{FW}} - E_b^{\text{BW}} = -2$  eV indicates that this model satisfies the detailed balance.

numerical method, the energy barrier as a function of  $\Delta E$  can be obtained as shown in Fig. 2(b).

Now that we have obtained function  $f(E_b^0, \Delta E)$ , the task of the energy barrier calculation has been converted to the task of computing  $E_b^0$  and  $\Delta E$  between metastable states. For  $E_b^0$ , the values in the non-interacting model [21] are used in this paper. However,  $\Delta E$  still needs to be calculated at every kMC step.

### 2.3. Cluster Expansion Method

DFT calculations can be used to compute the energy of different ionic configurations by solving for the electronic ground state of the system. DFT calculations are considered to be highly accurate and widely applicable, but are also computationally very expensive. For a system containing  $N$  electrons, the computational time of DFT scales as  $O(N^3)$ .

Even though the recent progress in the combination of high performance computing and DFT methods enables us to calculate the energy for larger systems (up to a few

hundred ions), the computation is still very expensive. For example, one DFT based structural relaxation calculation for about 300 ions in this paper takes about 3 days on 160 CPU's. Thus, it is impossible to do one such DFT calculation at every kMC step and we need an efficient method to predict the energy of arbitrary ionic configurations based on a limited set of DFT data. The cluster expansion method (CEM) enables us to reduce the computational load dramatically by avoiding the necessity of performing one DFT calculation for every ionic configuration.

In the CEM, the configurational properties of system are expanded with the orthonormal basis functions which are defined by the ionic configurations on the lattice. [35] Once we fit the expansion coefficients to a limited number of DFT calculations, these coefficients can be used to predict the energy of new ionic configurations. The cluster expansion method provides the basis functions for the expansion.

Consider an ionic configuration of YSZ which contains  $N$  lattice sites. In YSZ, four kinds species can occupy the lattice sites – they are host cation (Zr), dopant cation (Y), anion (O), and anion vacancy (VA) in YSZ. For simplicity we can assume that cations and anions exist only on their own sublattices: Zr and Y exist on the cation sublattice while O and VA exist on the anion sublattice. The ion type in each sublattice is labeled by a spin  $\sigma_i$ : +1 for Zr, -1 for Y, +1 for O, and -1 for VA in YSZ. Then the ionic configuration of a YSZ single crystal can be represented by a vector  $\vec{\sigma} = (\sigma_1, \sigma_2, \dots, \sigma_N)$ , where  $N$  is the number of lattice sites.

The cluster functions are defined as  $\phi_\alpha = \prod_{i \in \alpha} \sigma_i$ , where  $\alpha$  indicates a cluster composed of multiple lattice sites including empty cluster,  $N$  point clusters,  ${}_N C_2$  pair clusters,  ${}_N C_3$  three-body clusters, ..., and  ${}_N C_N$   $N$ -body cluster where  ${}_N C_m = \frac{N!}{m!(N-m)!}$ . These cluster functions satisfy the orthonormality condition,  $\langle \phi_\alpha \phi_\beta \rangle = \frac{1}{2^N} \sum_{\vec{\sigma}} \phi_\alpha \phi_\beta = \delta_{\alpha\beta}$  where the sum is over all possible choices of  $\vec{\sigma}$ . Because the cluster functions satisfy the condition of a orthonormal basis, the energy of a system can be expressed as a unique expansion of the cluster functions  $\phi_\alpha$ .

$$E(\vec{\sigma}) = \sum_{\alpha} V_{\alpha} \phi_{\alpha}(\vec{\sigma}) \quad (1)$$

where the coefficient  $V_{\alpha}$  associated to  $\phi_{\alpha}$  is called the effective cluster interactions (ECI) of cluster  $\alpha$ , and the sum is over all  $2^N$  cluster functions. We can obtain  $\phi$  and  $E$  from pre-computed DFT datasets. ECI then can be calculated from the least square solution of Eq.(1). Once ECI are obtained, the energy for any given  $\vec{\sigma}$  can be predicted by Eq.(1).

To prepare pre-computed DFT datasets, we performed DFT calculations for 140 different ionic configurations at the same doping concentration at 9 mol%, using the Vienna Ab-initio Simulation Package (VASP). [37, 38, 39, 40] GGA-PW91 scheme [41, 42] is used for exchange-correlation function and pseudopotentials with projector augmented wavefunctions (PAW) [43, 44] are used. All ions are allowed to move freely during the conjugate gradient relaxation.

§ This definition of basis functions is derived from the Chebyshev polynomials. [36]

The size of supercell used in this work is  $3[100] \times 3[010] \times 3[001]$ , which contains 108 cations (Cat) and 216 anions (An). This size is much larger than the supercell in previous DFT calculations of YSZ [21, 23, 45], and it can cover the 9th nearest neighbor (9NN) for Cat-An, 9NN Cat-Cat, and 18NN Cat-An. Because the size of supercell is large, gamma point is enough for the  $k$ -point sampling. The charge smearing factor SIGMA = 0.05 is used. Each configuration usually takes 3 days for full relaxation (volume and shape relaxation) on 160 CPU's. This high computational cost in DFT calculations is the main reason that we want to develop a cluster expansion model to predict the energies of arbitrary ionic configurations. The mean value of the energy in these 140 configurations is  $-2974.15$  eV and the standard deviation is 1.06 eV.

To solve Eq.(1) by the least square method, the number of dataset must be greater than or equal to the number of coefficient. There are  $2^{108} \times 2^{216} = 2^{324} \simeq 3.417 \times 10^{97}$  clusters in the  $3[100] \times 3[010] \times 3[001]$  YSZ supercells. Since the number of datasets, 140, is much smaller than the number of cluster functions, we need to truncate the clusters. The clusters in the supercell can be classified by their translational and rotational symmetries. Periodic boundary conditions limit the distance between two ions in a cluster within the half length of the supercell in all directions. Thus, a cut-off distance of  $1.5a_0$  is applied to all three dimensions. We also limit the number of ions in the cluster to be less than 4.

There are two types of point clusters, one is the cation point cluster and the other is the anion point cluster. For the anion-anion pair clusters, the independent clusters (not related by symmetry) are specified not only on by the distance between anions but also by the number of cations between the anions pair. The three-body clusters can be represented as a triangle, consisting of three line segments. Because each segment can be associated with a pair cluster, three-body clusters can be labeled by the set of three pair clusters. All pair clusters and one example three-body cluster are shown in the auxiliary material.

As a result of the above truncation schemes, the total number of independent ECI is 192. For robust fitting, the number of pre-computed datasets needs to be several times larger than the number of clusters. [46] Therefore we need to truncate the clusters further.

Among the 192 clusters, we select a small subset of clusters by minimizing the cross validation score (cvs). [47] As the quality of the selected clusters depends on the size of subset,  $k$ , we need to decide the optimal value for  $k$  itself. When the number of coefficient is too large and approaching to the number of pre-computed datasets, the clusters' ECI can be over-fitted meaning that the fitting error is very small but the fitted model will make huge errors in making new predictions. (See the Supplement Material for the demonstration of the dependence of the predictive power on  $k$ .) Thus it is necessary to check whether the fitted coefficients have any predictive power. We can measure the predictive power from the error in the prediction of the energy of new ionic configurations which are not included in the fitting. Among the 140 datasets, 100 datasets are used for fitting of ECI and the remaining 40 datasets are used for checking



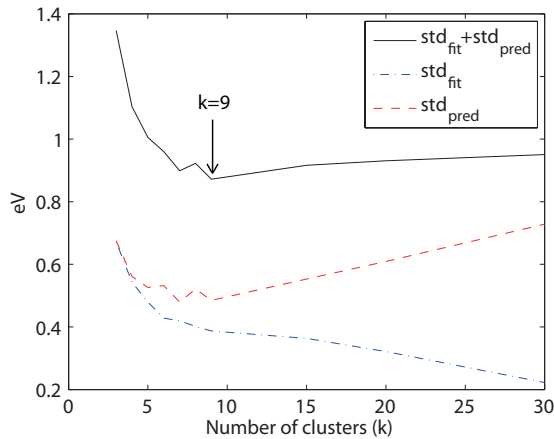


**Figure 3.** Standard deviation in fitting and real prediction for different  $k$ .

Cluster	Ion 1	Ion 2	Ion 3	ECI (eV)
0	0, 0, 0			-15.1704
1	1, 1, 1	-1, 1, 1	1,-1, 1	0.0288
2	1, 1, 1	-1,-1,-1	-1,-1, 3	0.0113
3	0, 0, 0	-3,-1,-1	1,-5,-1	-0.0059
4	1, 1, 1	-2, 0, 0	-4, 2, 4	-0.0047
5	1, 1, 1	-2, 0,-2	-2, 4,-2	0.0058
6	1, 1, 1	-2, 0,-2	-4, 2, 2	-0.0074
7	1, 1, 1	-4, 0, 0	0,-4, 0	0.0057
8	0, 0, 0	0,-2,-2	4, 2,-2	0.0028

**Table 1.** The ionic configuration of selected 9 clusters and corresponding ECI's

the predictive power of the fitted ECI.

A reasonable approach to assess whether or not over-fitting occurs is to compare the standard deviation in the error ( $E_{\text{DFT}} - E_{\text{CEM}}$ ) for the two data sets used in fitting and in testing real predictions, respectively. For a fixed  $k$ , Monte Carlo algorithm is used to search a set of  $k$  clusters providing the lowest cvs. This process is repeated by changing  $k$  systemically. Standard deviations of the error in fitting and in real prediction for different  $k$  are obtained as shown in Fig. 3. From this result, we conclude that  $k=9$  is optimal, because the summation of two standard deviations is minimized when  $k=9$ . It also implies that in this case the optimized ratio between the size of cluster set and the number of datasets is close to 0.1(=9/100). When the selected 9 clusters are used to predict the energy of 40 datasets which are not included in the fitting, the result is given in Fig. 4. The root-mean-square (RMS) error in real prediction is 0.0049 eV per cation, which is consistent or even smaller compared with previous works. [45]

One of the 9 clusters is a cation point cluster, representing the cohesive energy of the YSZ crystal. The ionic positions of remaining 8 clusters are given in Table 1. It is interesting that all the selected clusters (except the point cluster) are three-body

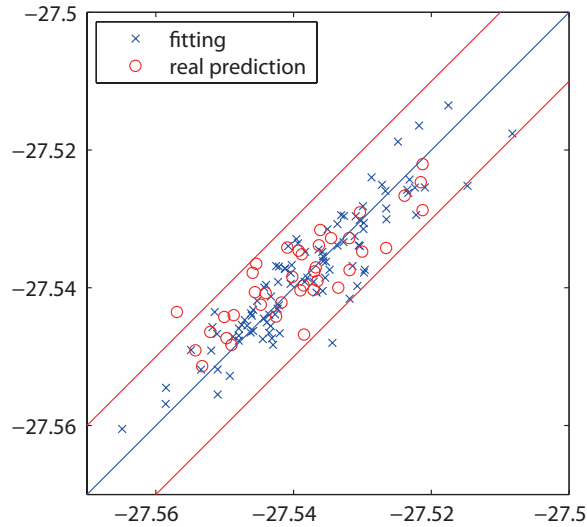


**Figure 4.** Correlation between DFT calculations ( $x$ -axis) and real prediction by CEM ( $y$ -axis) when  $k=9$  in terms of energy per cation (eV). The blue line corresponds to  $E_{\text{DFT}} = E_{\text{CEM}}$ . Red lines correspond to the tolerance of  $\pm 0.01$  eV in terms of energy per cation.

clusters. In empirical potential models, the ionic interaction has been usually considered to be dominated by pair interactions and three-body terms are often considered as higher order corrections. The previous works using cluster expansion method also reported that pair clusters are selected more frequently than three-body clusters and have stronger ECI's. [45]

The difference with previous works may originate from the fact that the number of selected clusters  $k$  in previous works is substantially larger than what we use ( $k = 9$ ) in this paper. The other possible reason is the purpose of the fitted CEM model. Previous works aim to the energy and structure of the ground state, while the aim in this paper is to predict the energies of all the meta-stable states encountered in kMC simulations of vacancy diffusion. Pair clusters may be more important for predicting ground state energies and three-body clusters may be more important for meta-stable states.

The ECI's obtained for the selected clusters, except the cation point cluster, are given in Table 1. The ECI corresponding to the cation point cluster is not relevant for kMC simulations of ionic conduction because it contributes the same constant to all meta-stable states. Similarly, the ECI corresponding to CCC cluster also cancels out in the energy difference, because cations don't move in our kMC simulations. ECI's of the selected clusters are not strongly correlated with the size of the clusters.

Using the fitted ECI's, the binding energy between Y ion and oxygen vacancy can be obtained. The energy of system with one Y ion and one vacancy ( $E_{1V1Y}$ ) is calculated by changing the position of vacancy with respect to Y ion ( $d_{YV}$ ). This energy is then compared with the energies of a crystal containing one Y ion ( $E_{1Y}$ ), of a crystal containing one oxygen vacancy ( $E_{1V}$ ), and of a pure zirconia crystal ( $E_{00}$ ).

$$E_{\text{bind}}(x) = E_{1V1Y}(x) - E_{1Y} - E_{1V} + E_{00} \quad (2)$$

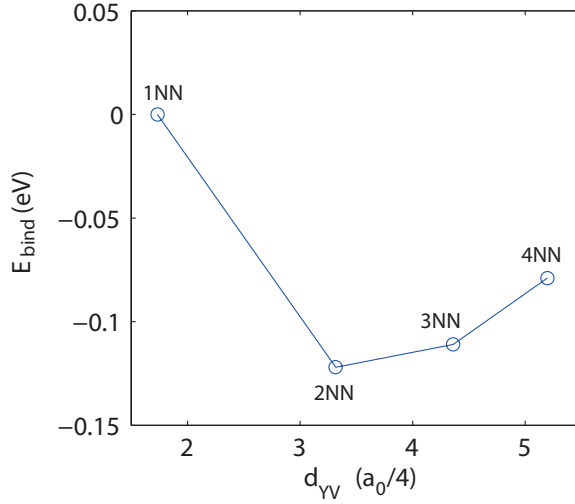


**Figure 5.** Binding energy between one Y ion and one vacancy.  $x$  axis is the distance between the vacancy and the Y ion.  $n$ NN indicates the  $n$ -th nearest neighbor relation between the vacancy and the Y ion.

	$\Delta E$	$E_b^0$	$E_b^{\text{DFT}}$	$E_b$
1	0.32	0.58	0.65	0.67
2	-0.52	1.29	1.10	0.98
3	-0.44	1.86	1.40	1.45

**Table 2.** Comparison between the energy barrier prediction by a direct DFT calculation ( $E_b^{\text{DFT}}$ ) method and our model ( $E_b$ ), in three sampled cases.

The result is plotted in Fig. 5. We can see that the vacancy prefers to be located at the second nearest neighbor site of Y ion. This behavior of binding energy is consistent with the previous works where the binding energy was calculated by fitting to several DFT calculations [22, 23, 48] and also is consistent with experiments. [49, 50, 51]

We recall that  $E_b$  is predicted as a function of the calculated  $\Delta E$  and  $E_b^0$ , using the function illustrated in Fig. 2(b). In this paper,  $E_b^0$  is taken as the same values in the non-interacting model [21], where  $E_b^0$  is assumed to depend on the two cations on the transition plane:  $E_b^0$  is 0.58 eV for Zr-Zr pair, 1.29 eV for Y-Zr pair, and 1.86 eV for Y-Y pair, respectively. We examined three sampled cases to compare the  $E_b$  prediction by our model with that by a direct DFT calculation. For a direct DFT calculation, the constrained minimization method and the  $3[100] \times 3[010] \times 3[001]$  supercell were used. The result, given in Table 2, shows that the discrepancy between our model and a direct DFT calculation is within  $\sim 0.12$  eV.

### 3. Effect of doping concentration

Using the cluster expansion and energy barrier models described above, KMC simulations are performed to study how the electrical impedance of the YSZ single

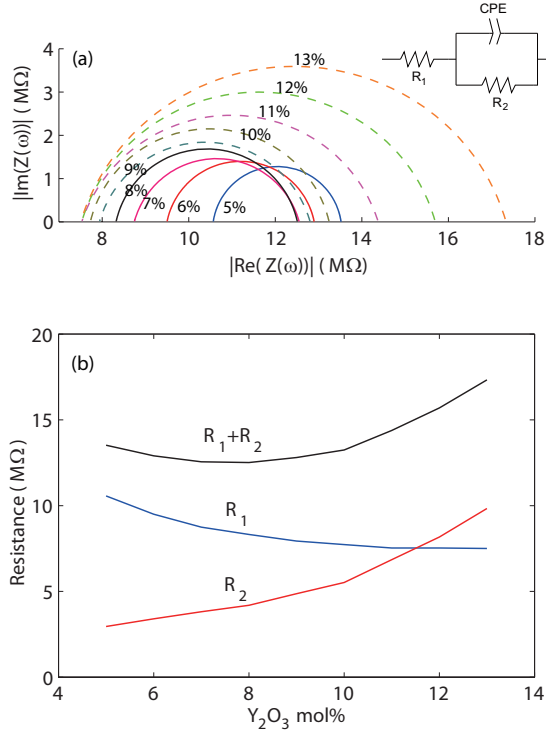


**Figure 6.** (a) The Nyquist plot at different doping concentration for the interacting model. (b) Equivalent circuit parameters when the doping concentration changes – the energy barrier model is the interacting model. The summation of  $R_1$  and  $R_2$  is the resistance at zero frequency and becomes minimum (or maximum conductance) at 8 mol%. Notice that all these calculations were performed at  $T = 1800$  K.

crystal changes as the doping concentration changes. A  $3[100] \times 3[010] \times 3[001]$  supercell is used and the temperature is set to 1800 K. Doping concentration changes from 5 mol% to 13 mol%. To represent the random Y distribution in the bulk YSZ, 40 different distributions of yttrium ions are sampled for one doping concentration. Due to the interactions between ions, each ion will have an optimal position that minimizes the total energy. Thus there exists a transient period until the system reaches a steady state. The transient period is set to  $6 \times 10^5$  kMC jumps. In our previous work [52], we developed an efficient method using the fluctuation-dissipation theorem to calculate the electrical impedance from kMC simulation. The same method is used in this paper to calculate the impedance in  $x$ -direction. The results are given in Fig. 6(a).

The shape of the Nyquist plot is approximately an arc, so it is fitted to the equivalent circuit model shown in the inset of Fig. 6(a), which contains two resistances ( $R_1$  and  $R_2$ ) and one Constant Phase Element (CPE). [53]  $R_1$  is a pure resistance corresponding to the resistance at the infinite-frequency limit,  $R_2$  corresponds to the width of the arc.  $R_2$  and CPE together determines the shape of the arc.  $R_1 + R_2$  is the resistance at zero frequency. The total impedance of this equivalent circuit is

$$Z(\omega) = R_1 + \frac{R_2}{1 + R_2 Q(j\omega)^\alpha} \quad (3)$$

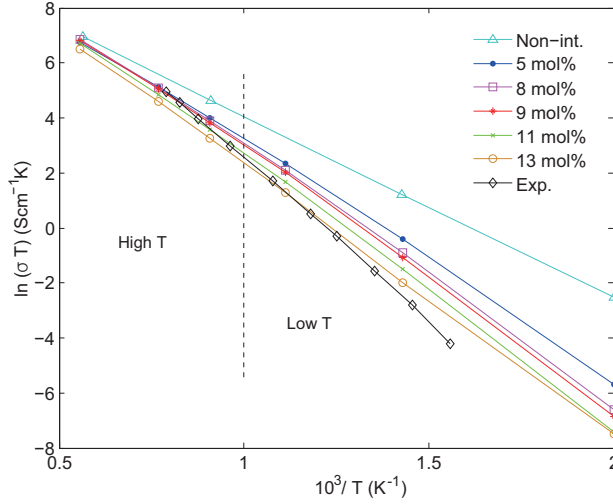


**Figure 7.** Temperature dependence of the conductivity at different doping concentrations with randomly distributed Y ions. Non-int: Prediction of the ionic conductivity at 8 mol% by the non-interacting model. Exp: Experimental data of the ionic conductivity at 8 mol% reproduced from Ref. [54], which shows that the ionic conductivities predicted by our model are in the same range as an experimental data in overall scale.

The left end of the arc ( $R_1$ ) continuously decreases as the doping concentration increases, while the width of the arc ( $R_2$ ) continuously increases as shown in Fig. 6(b). Thus the summation of  $R_1$  and  $R_2$  becomes minimum at an optimum doping concentration. The predicted doping concentration is 8 mol%, which is consistent with 8 mol% of the experimental observations at high temperatures. [54]

The electrical conductivity  $\sigma$  is  $\frac{l_x}{l_y l_z} \frac{1}{R_1 + R_2}$ , where  $l_x$ ,  $l_y$ , and  $l_z$  are the length of the supercell in  $x$ ,  $y$ , and  $z$  direction, respectively. The conductivities at 5, 8, 9, 11, and 13 mol% doping concentrations are obtained at temperature of 500, 700, 900, 1100, 1300 K and 1800 K. From this result, the temperature dependence of conductivity is plotted in Fig. 7. It is interesting that the  $\sigma$  at 5 mol% is greater than the  $\sigma$  at 8 mol% when the temperature is lower than 1300 K. The shift of optimal concentration to the lower values at lower temperatures also appears in previous non-interacting model [21] as well as in some experimental data. [54] The  $\sigma$  is usually expressed as

$$\sigma = \frac{A_0}{T} \exp \left[ \frac{-E_b^{\text{eff}}}{k_B T} \right] \quad (4)$$

where  $E_b^{\text{eff}}$  is the effective energy barrier and  $A_0$  is a constant. Hence, the effective energy barrier is obtained from the temperature dependence of conductivity. The result is given in Table 3. Although the experimental data are also scattered in the range of 0.74–1.1 eV [55, 56, 57] so that the exact value of effective energy barrier is unknown, the overall trend of the increased effective energy barrier with lower temperature or higher doping concentration commonly appear in the experimental data as well as in our prediction, as shown in Fig. 8.

Dop. (mol%)	high $T$	low $T$	overall
5	0.69 eV	0.78 eV	0.74 eV
8	0.74 eV	0.85 eV	0.81 eV
9	0.74 eV	0.86 eV	0.82 eV
11	0.76 eV	0.88 eV	0.85 eV
13	0.81 eV	0.85 eV	0.84 eV

**Table 3.** Effective energy barrier obtained from Fig. 7 – high  $T$  range indicates  $T > 1000$  K, low  $T$  range indicates  $T < 1000$  K, and overall indicates the entire temperature range (500–1800 K).

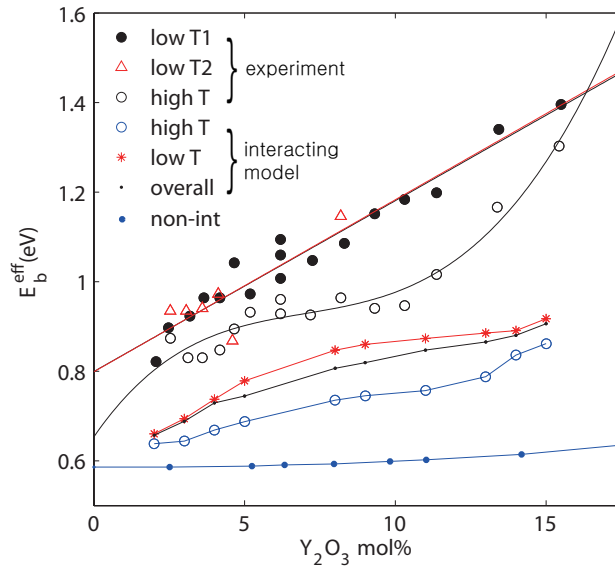


**Figure 8.** Effective energy barrier as a function of doping concentration predicted by the interacting model. Experimental data for comparison is reproduced from Ref. [54]. ●: low temperature region determined by four-probe a.e. method, △: low temperature region determined by complex impedance method, ○: high temperature region determined by four-probe a.c. method. non-int indicates the prediction by non-interacting model and is reproduced from Ref. [21].

The pre-factor  $A_0$  in Eq. (4) can also be obtained from the temperature dependence of the conductivity. Fig. 9 shows that  $A_0$  decreases as the doping concentration decreases below 10 mol%. This can explain the low conductivity at low doping concentrations despite the low effective energy barrier at low doping concentrations. According to the Nernst-Einstein relation,  $A_0$  is proportional to the density of the charge carrier. Thus the decrease of conductivity at very low doping concentration is caused by the lack of charge carriers. At very high doping concentration, the conductivity decreases because oxygen vacancy jumps are more likely to experience higher energy barriers due to their interactions with Y cations.

In previous KMC models, the predicted absolute conductivity is often not compared with the experimental observations, because an empirical constant  $\nu$  (jump trial

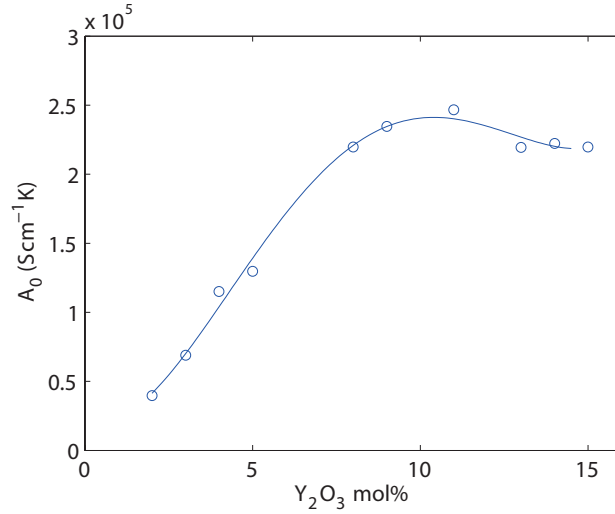


**Figure 9.** Prefactor  $A_0$  of the conductivity as a form of  $\sigma = \frac{A_0}{T} \exp\left(-\frac{E_b}{k_B T}\right)$ .

frequency) is used commonly in all the probability rates and, in turn, the conductivity is linearly scaled by  $\nu$ . Nonetheless, theoretical estimate of  $\nu$  exists [58] and it is important to check whether the theoretical predictions on the absolute values of the conductivity are comparable with experiments. For example, our prediction of the conductivity at  $T = 1273$  K, which is predicted to be 0.11 (S/cm) as shown in Fig. 7. The corresponding experimental observation at  $T = 1273$  K is 0.10 (S/cm).

#### 4. Effect of dopant distribution

In the following, the kMC model is used to study the effect of dopant distribution on ionic conductivity. A key question to be addressed is whether there exist an optimal dopant distribution that maximizes ionic conductivity. We will examine the behavior of several hypothetical dopant distributions. Again, the  $3[100] \times 3[010] \times 3[001]$  supercell is used and the doping concentration is set to 9 mol%.

##### 4.1. Spherical distribution

In the first hypothetical distribution, a fraction  $x$  of Y ions segregate forming a spherical cluster and the remaining Y ions are randomly distributed in the supercell. We calculate the impedance by changing the fraction of segregated Y ions. The initial positions of vacancies are randomly distributed and data collection starts after a transient period of  $6 \times 10^5$  kMC jumps to reach equilibrium. 80 million kMC jumps at 1800 K are performed for each distribution. The results are shown in Fig. 10(a). We observe that segregation of Y ions into a sphere only increases the electrical impedance (*i.e.* decreases the ionic conductivity) of YSZ. To gain insight on the microscopic mechanisms, we examine the dependence of various parameters of the equivalent circuit on dopant concentration.

When the Nyquist plots are fitted to a two-arcs model,  $R_3$  is always much smaller

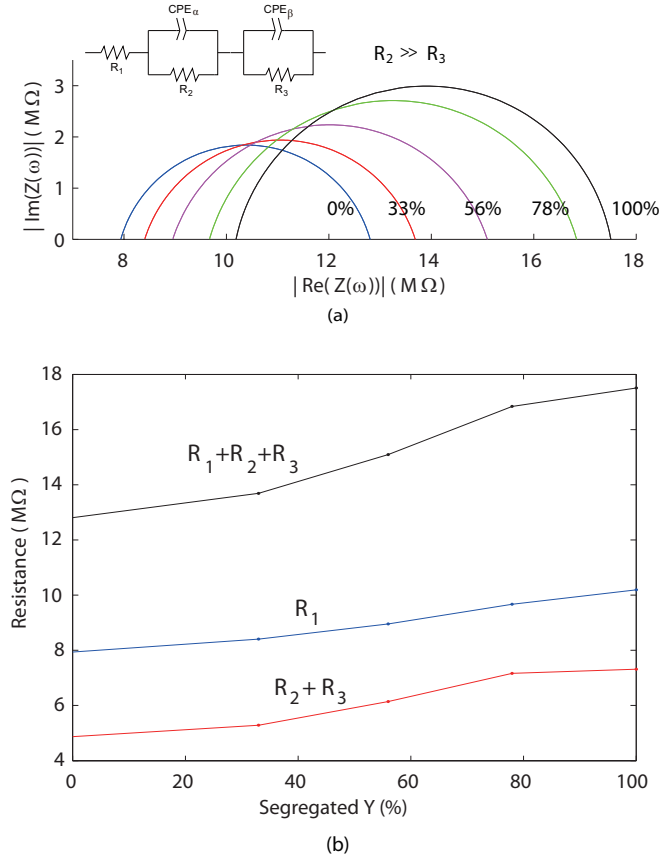


**Figure 10.** (a) Nyquist plot of YSZ cystral when different ratio of Y ions are segregated forming a spherical clusters. (b) Equivalent circuit parameters when different ratio of Y ions are segregated forming a spherical clusters.

than  $R_2$  (by two orders of magnitude). This supports that the Nyquist plot has a single arc shape. In the following, we still use the equivalent circuit with two arcs to fit the impedance spectrum.  $R_1$  corresponds to the left end of the arc and  $R_2 + R_3$  corresponds to the width of the arc. The equivalent circuit parameters as functions of the fraction of segregated Y ions are plotted in Fig. 10(b). We can see that both  $R_1$  and  $R_2 + R_3$  increase when more Y ions are segregated.

The hypothetical Y-segregation was intended to enhance the ionic conductivity by providing Y-free regions, which has low energy barrier for the diffusing vacancy. KMC simulations based on the non-interacting model have predicted that such a structure would enhance ionic conductivity. [52] However now the interacting model predicts that Y-segregation forming a spherical cluster is detrimental to ionic conductivity. The origin of this discrepancy between the predictions by the interacting model and by the non-interacting model can be explained in terms of the vacancy distribution. Recall that the vacancy concentration and the effective energy barrier together determine the conductivity. [59] In the case of the non-interacting model, all meta-stable states have identical energy, which leads to a uniform vacancy distribution despite of the existence of the interaction between the vacancy and cations. However, in the interacting model, the



vacancy distribution will no longer be uniform if the Y ions are not randomly distributed.

We obtained the vacancy distribution using the simulated annealing method and observed that the energetically favorable positions of the vacancies are at the first nearest neighbor of outer Y ions of the spherical Y cluster. To diffuse over long distances and contribute to the ionic conductivity, vacancies must detach from the Y clusters. This requires overcoming a binding energy of about 0.12 eV (Fig. 5), which reduces the ionic conductivity. Therefore the reduction of ionic conductivity is caused by the increase of spatial variation of the interaction energy. This finding explains why the non-interacting model is quite successful when the Y ion distribution is completely random, but experiences problems as soon as this is not the case.

Let us return to the change of the equivalent circuit parameters with the fraction of segregated Y ions in spherical distribution. As more Y ions are segregated, vacancy concentration becomes higher near the Y-sphere, which leads to more vacancy-vacancy and vacancy-yttrium interactions. We propose that the increased ionic interactions is the cause of increase of  $R_2 + R_3$  with increasing Y segregation (Fig. 10(b)), similar to the increase of  $R_2$  with increasing doping concentration (Fig. 6(b)). We propose that  $R_1^{-1}$  is proportional to the vacancy concentration in Y-free region (i.e. mobile vacancy concentration).

#### 4.2. Layered distribution

Following the reasoning given above, we might expect a different result when Y ions are segregated to a layer, because intuitively it provides the diffusing channels without requiring oxygen vacancies to detach from isolated Y clusters. In these channels, vacancies jumping along a direction parallel to the Y layer experience a reduced spatial variation of the energy. We tested configurations where Y ions are segregated to a layer parallel to the  $x$  axis (conduction direction) in  $3[100] \times 3[010] \times 3[001]$  supercell. To minimize the reduction of spatial variation of the energy, all cation sites in the segregation layer are completely occupied by Y ions, which corresponds to 9 mol% of doping concentration. 800 million kMC steps are performed at  $T = 1800$  K. The conductivity is predicted to be 0.21 S/cm, while it is 0.51 S/cm and 0.37 S/cm for the random distribution and the spherical cluster, respectively. Unfortunately, the interacting model predicts that the ionic conductivity when Y ions segregate to a layer is still lower than when the Y ions are randomly distributed.

Using the simulated annealing method, the optimal vacancy distribution is obtained when Y ions are segregated to a layer. We observe that vacancies are located in the first anion layer next to the Y-segregation layer. The vacancy distribution at finite temperatures will not be very different from the minimum-energy vacancy distribution. Hence, when a vacancy jumps in  $x$  direction, it mostly experiences a Y-Zr pair ( $E_b^0 = 1.29$  eV) at its saddle configuration, which results in high  $E_b$ . This region can be called slow diffusing channels while the region where a jumping vacancy experiences Zr-Zr pair ( $E_b^0 = 0.58$  eV) can be called fast diffusing channels.

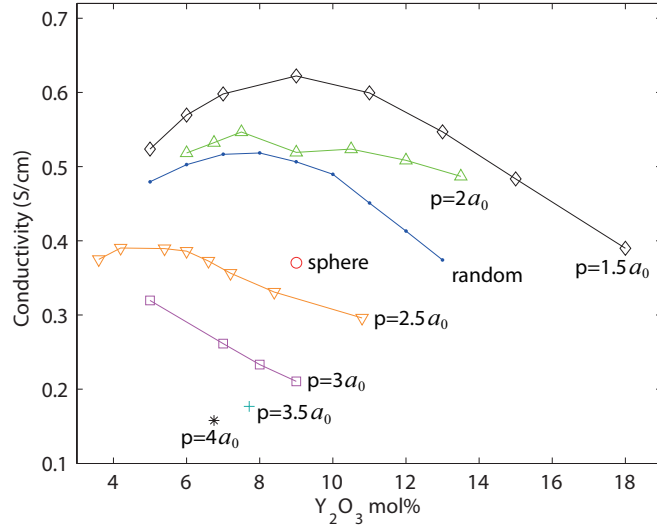


**Figure 11.** Ionic conductivity in different layer structures at  $T = 1800$  K. Conductivities of random distribution and spherical cluster are plotted for comparison.

When all the cation sites in one layer are occupied by Y, we have seen that excessive Y-segregation in this layer attracted vacancies to the first anion layer and this lowers ionic conductivity. The number of vacancies in the first anion layer could be reduced by reducing the number of Y ions in the segregation layer. Another factor to determine the conductivity of layer structure is the distance between adjacent Y layers. As more Y-segregation layers are accommodated in the supercell, the vacancy concentration increases and ionic conductivity may be enhanced. However, too short inter-layer distance may cause more vacancies to get too close to the Y layers and to reduce ionic conductivity.

Various layered structures are examined to verify the hypothesis that two factors determine the ionic conductivity in a layer structure: the number of Y ions in the segregation layer and the period of the segregation layer. Layer structures in a  $3[100] \times 3[010] \times (p/a_0)[001]$  supercell are prepared by changing the number of Y ions in the segregation layer and by changing the inter-layer distance  $p$ . In all cases Y ions are randomly distributed in the segregation layer. Since Y ions are located in the segregation layer only, doping concentration changes according to the number of Y ions in the segregation layer. 800 million kMC jumps are performed at 1800 K and the results are shown in Fig. 11.

We observe that the ionic conductivity is maximized at 9 mol%, when  $p=1.5a_0$ . At this doping concentration, half of cation sites in the segregation layer are occupied by Y ions. The effective energy barrier of the entire structure can be obtained from the temperature dependence of ionic conductivity. The optimal distribution, the Y-segregation layer structure at 9 mol% with  $p=1.5a_0$ , is examined. The effective energy barrier of this structure is obtained as 0.74 eV for  $T > 900$  K and 0.85 eV for  $T < 900$  K, which is very close to the effective energy barrier in random Y distribution case. This similar effective energy barrier results in very small enhancement of the ionic conductivity. The conductivity is enhanced by only 20% at  $T = 1800$  K and 17% at

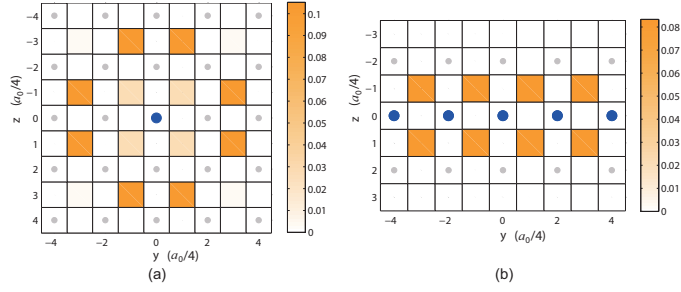


**Figure 12.** Vacancy distribution at 500 K – (a) vacancy distribution around Y-segregation line (b) vacancy distribution when the spacing between two consecutive segregation lines is zero. The segregation line is laid in  $x$ -direction. Blue circles indicate Y ions in the segregation lines and gray circles indicate Zr ions. Darker yellow color means higher vacancy concentration. In the segregation line, all cation sites are occupied by Y ions.

$T = 500$  K, compared with random Y distribution at 8 mol% of doping concentration.

The reason of this low enhancement can be explained by the destruction of fast diffusing channels. We removed some Y ions in the segregation layer to reduce vacancy attraction to the first anion layer, but random removal of Y ions increases the spatial variation of the potential energy in the ionic conduction direction. The energy fluctuation in the interaction energy increases the energy barrier of the jumping vacancies.

#### 4.3. Linear distribution

If Y ions are distributed in a line in  $x$ -direction, a vacancy jumping in the  $x$ -direction will not experience any energy variation as well as the number of Y ions in the segregation layer is reduced. All cation sites in the segregation line need to be completely occupied by Y ion for the energy variation to vanish. The energy of a hypothetical system, which has one Y-segregation line in the  $x$ -direction and one oxygen vacancy, is calculated by changing the vacancy position in  $(y, z)$  space. The vacancy concentration in  $(y, z)$  space can be approximated by the Boltzmann factor using this energy. The result at  $T = 500$  K is plotted in Fig. 12(a). We can clearly see that the vacancy concentration is high in fast diffusing channels, where a vacancy jumping in  $x$ -direction experiences a Zr-Zr pair only and  $\Delta E$  by vacancy-cation interactions is zero. As more Y-segregation lines are accommodated in the supercell, more vacancies are created and the ionic conductivity should increase.

However, some minimum spacing between Y-segregation lines is required. Otherwise, we get to the same planar segregation in the limit of inter-rod spacing going to zero. In that case, as shown in Fig. 12(b), the vacancy concentration is the highest at the first anion layer, in which vacancy experiences Zr-Y pairs (high  $E_b^0$ ) when jumping in the  $x$ -direction. On the other hand, if the spacing is too wide, the ionic conductivity will also be low due to insufficient oxygen vacancy concentration. Thus there must exist

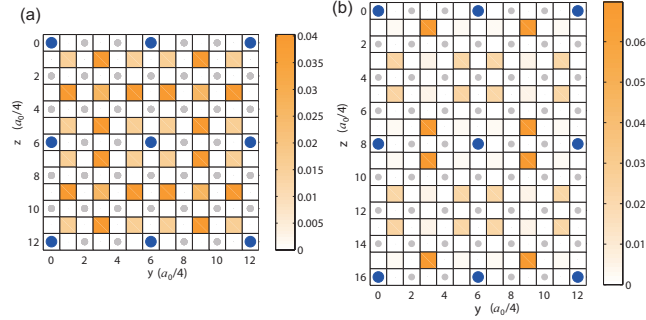


**Figure 13.** Vacancy distribution in (a) structure A at 1800 K (b) structure B at 500 K. Blue circles indicate Y-segregation lines and gray circles indicate Zr ions. Darker yellow color means higher vacancy concentration. In Y-segregation line, all cation sites are occupied by Y ions.

Structure	$T > 900$ K	$T < 900$ K	overall
A	0.63 eV	0.71 eV	0.68 eV
B	0.60 eV	0.64 eV	0.63 eV
random (8 mol%)	0.74 eV	0.85 eV	0.81 eV

**Table 4.** Effective energy barrier of structure A and structure B.

an optimal spacing between Y-segregation lines. From Fig. 12(a), we can infer that the promising candidates of optimal spacing are  $1.5a_0$  and  $2a_0$ .

To search for the optimal microstructure, several 2D superlattices are tested. We examined three cases of spacing between Y-segregation lines –  $(1.5a_0, 1.5a_0)$ ,  $(1.5a_0, 2a_0)$ , and  $(2a_0, 2a_0)$  for  $y$  and  $z$  directions. After 800 million kMC steps, the conductivity at each spacing is calculated as 69.71, 58.72, and 35.27 ( $\text{S}/\text{cm}^{-1}$ ) at  $T = 1800$  K and 0.0029, 0.0059, and 0.0012 ( $\text{S}/\text{cm}^{-1}$ ) and at  $T = 500$  K. This means that the optimal spacing is  $(1.5a_0, 1.5a_0)$  at  $T = 1800$  K and  $(1.5a_0, 2a_0)$  at  $T = 500$  K. We will call these structures A and B, respectively. Vacancy distribution is obtained by statistically collecting the positions of all vacancies at all kMC steps. The results are shown in Fig. 13. We can see that in both structures the vacancy concentration is high at fast diffusing channels.

Structure A and B corresponds to 6 mol% and 4.5 mol% of doping concentration, respectively. Lower doping concentration in structure B leads to less vacancy-vacancy interactions, which helps to decrease the effective energy barrier in structure B. The temperature dependence of conductivity for each structure is given in Fig. 14. Structure A has higher conductivity at  $T > 900$  K, while the structure B has higher conductivity  $T < 900$  K. From this result, the effective energy barriers can be extracted and are listed in the Table 4. We can see that the effective energy barrier of structure B is always less than that of structure A as expected. Both structure A and B show enhanced ionic conductivity compared with the structure with random Y distribution at 8 mol% of doping concentration as given in Table 5.

It may seem difficult to manufacture these two structures using today's synthesis

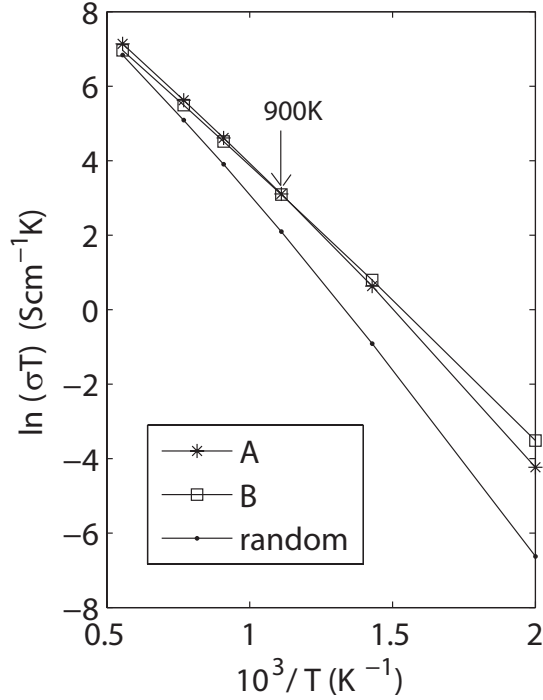


**Figure 14.** Temperature dependence of the ionic conductivity in structure A and B are compared with the structure with randomly distributed Y ions.

Structure	$T = 1800$ K	$T = 500$ K	$T = 300$ K
A	1.35	11	86
B	1.15	22	532

**Table 5.** Enhancement factor, defined as  $\sigma/\sigma_{\text{random}}$ , of ionic conductivity for structure A and structure B.

techniques. However, The field of nano-fabrication is advancing very fast. Many bottom-up or top down techniques are continuously added to our repertoire to fabricate more and more complex nano-structures. Moreover, the same method described here can be applied to predict the optimal structure of other solid electrolyte material such as Gadolinium-doped Ceria (GDC). If the optimal structure in other electrolyte materials were such that dopant ions segregate into planes, it would then be quite straightforward to synthesize by existing technologies such as molecular beam epitaxy (MBE) and atomic layer deposition (ALD). [60, 61, 62]

## 5. Conclusion

In this paper, a kinetic Monte Carlo (kMC) model is developed to simulate the vacancy diffusion in single crystal bulk Ytria-stabilized Zirconia (YSZ). As the energy barrier is essential input to kMC simulation, accurate and efficient energy barrier model is required. To improve the energy barrier model, we used cluster expansion method to account for the ionic interactions. The parameters in the cluster expansion method are

fitted to 100 data points of density functional theory (DFT) calculations using relative large (324 ions) supercells. Care has been taken to ensure the robustness of the fitting and the predictive power of the fit is verified over 40 data points not included in the fitting. Developed kMC model is applied to calculate the ionic conductivity at various microstructures, which helps to understand the mechanisms of the ionic conduction in YSZ.

Our kMC model predicts the electrochemical impedance spectroscopy (EIS) spectrum of the YSZ crystal, which helps to separate the various contributions to the ionic conductivity. When Y ions are randomly distributed, the impedance is calculated at different doping concentration and temperature, and the conductivity can be obtained from the zero frequency impedance on the EIS spectrum. It is predicted that the conductivity is maximized at 8 mol% of doping concentration and the effective energy barrier is 0.74~0.81 eV, which are compatible to the experimental observations. The dependence of EIS spectrum on doping concentration shows that the density of charge carrier and the ionic interactions are two competing and quantifiable mechanisms to ionic conductivity.

The ionic conductivity is calculated for several structures with different dopant (Y) distributions. It is demonstrated that the ionic conductivity is dependent on both the vacancy distribution and the energy barrier. This result is then used to search for the optimal dopant distribution that maximizes ionic conductivity. The predicted optimal dopant distribution is the microstructure in which the Y ions segregation into a line parallel to the conduction direction, and arrange into a rectangular superlattice in the perpendicular directions. An optimal spacing between Y lines exists that balances the need to increase oxygen vacancy density and the need to avoid vacancy segregation to the first nearest neighbor to Y ions.

## References

- [1] J. B. Goodenough, *Annu. Rev. Mater. Res.* **33**, 91 (2003).
- [2] B.C.H. Steele, *Journal of Power Sources* **47**, 1 (1994).
- [3] J. Shim, C. Chao, H. Huang, and F. B. Prinz, *Chem. Mater.* **19**, 3850 (2007).
- [4] T. Sayle, S. Parker, and D. Sayle, *J. Mater. Chem.* **16**, 1067 (2006).
- [5] C. Korte, A. Peters, J. Janek, D. Hesse, and N. Zakharov, *Phys. Chem. Chem. Phys.* **10**, 4623 (2008).
- [6] Igor Kosacki, Christopher M. Rouleau, Paul F. Bechera, James Bentley, Douglas H. Lowndes, *Solid State Ionics* **176**, 1319 (2005).
- [7] X. Guo and J. Maier, *Adv. Mater.* **21**, 2619 (2009).
- [8] Shriram Ramanathan, *J. Vac. Sci. Technol. A* **27**, 1126 (2009).
- [9] G. Knoner, K. Reimann, R. Rower, U. Sodervall, and H. Schaefer, *Proc. Nat'l. Acad. Sci.* **100**, 3870 (2003).
- [10] R. De Souza, M. Pietrowski, U. Anselmi-Tamburini, S. Kim, Z. Munir, and M. Martin, *Phys. Chem. Chem. Phys.* **10**, 2067 (2008).
- [11] N. Sata, K. Eberman, K. Eberl, and J. Maier, *Nature* **408**, 946 (2000).
- [12] J. Garcia-Barriocanal, A. Rivera-Cvalzada, M. Varela, Z. Sefrioui, E. Iborra, C. Leon, S. J. Pennycook, and J. Santamaria, *Science* **321**, 676 (2008).

- [13] N. Schichtel, C. Korte, D. Hesse, and J. Janek, *Phys. Chem. Chem. Phys.* 11, 3043 (2009).
- [14] C. Korte, N. Schichtel, D. Hesse, and J. Janek, *Monatsh Chem* 140, 1069 (2009).
- [15] A. Kushima and B. Yildiz, *J. Mater. Chem.* 20, 4809 (2010)
- [16] T. Pennycook, M. Beck, K. Varga, M. Varela, S. Pennycook, and S. Pantelides, *Phys. Rev. Lett.* 104, 115901 (2010).
- [17] Fuyuki Shimojo and Hideo Okazaki, *Journal of the Physical Society of Japan*, 61, 4106 (1992).
- [18] Martin Meyer, Norbert Nicoloso, and Volker Jaenisch, *Physical Review B* 56, 5961 (1997).
- [19] P. Hohenberg and W. Kohn, *Phys. Rev.* 136, B864-B871 (1964).
- [20] W. Kohn and L. J. Sham, *Phys. Rev.* 140, A1133-A1138 (1965).
- [21] R. Krishnamurthy, Y.-G. Yoon, D. J. Srolovitz, and R. Car, *J. Am. Ceram. Soc.* 87, 1821 (2004).
- [22] Rojana Pornprasertsuk, PhD Thesis, Stanford University (2006).
- [23] R. Pornprasertsuk, P. Ramanarayanan, C. B. Musgrave, and F. B. Prinz, *J. Appl. Phys.* 98, 103513 (2005).
- [24] Rojana Pornprasertsuk, Jeremy Cheng, Hong Huang, and Fritz B. Prinz, *Solid State Ionics* 178, 195 (2007).
- [25] F. Pietrucci, M. Bernasconi, A. Laio, and M. Parrinello, *Phys. Rev. B* 78, 094301 (2008).
- [26] P.P. Dholabhai, S. Anwar, JB Adams, P Crozier, R. Sharma, *J. Solid State Chem.* 184, 811-817 (2011)
- [27] A. Van der Ven, G. Ceder, M. Asta, and P. D. Tapesch, *Phys. Rev. B* 64, 184307 (2001).
- [28] A. Van der Ven and G. Ceder, *Phys. Rev. Lett.* 94, 045901 (2005).
- [29] L. Semidey-Flecha and D. S. Sholl, *J. Chem. Phys.* 128, 144701 (2008).
- [30] A. Predith, G. Ceder, C. Wolverton, K. Persson, and T. Mueller, *Phys. Rev. B* 77, 144104 (2008).
- [31] E. Lee, F. B. Prinz, and W. Cai, *Phys. Rev. B (Brief Report)* 83, 052301 (2011).
- [32] M. Kalos and P. A. Whitlock, *Monte Carlo Methods Volume 1: Basics*, John Wiley & Sons (1986).
- [33] M. Putkonen, T. Sajavaara, J. Niinisto, L. Johansson, and L. Niinisto, *J. Mater. Chem.* 12, 442 (2002).
- [34] V. V. Bulatov and W. Cai, *Computer Simulations of Dislocations*, chapter 9, Oxford University Press (2006).
- [35] D. de Fontaine, *Solid State Physics* 47, 33 (1994).
- [36] R. Drautz, M. Fahnle, and J. M. Sanchez, *J. Phys.: Condens. Matter* 16, 3843 (2004).
- [37] G. Kresse and J. Hafner, *Phys. Rev. B* 47, 558 (1993).
- [38] G. Kresse and J. Hafner, *Phys. Rev. B* 49, 14251 (1994).
- [39] G. Kresse and J. Furthmuller, *Comput. Mat. Sci.* 6, 15 (1996).
- [40] G. Kresse and J. Furthmuller, *Phys. Rev. B* 54, 11169 (1996).
- [41] J.P. Perdew, J.A. Chevary, S.H. Vosko, K.A. Jackson, M.R. Pederson, D.J. Singh, and C. Fiolhais, *Phys. Rev. B* 46, 6671 (1992).
- [42] J.P. Perdew, J.A. Chevary, S.H. Vosko, K.A. Jackson, M.R. Pederson, D.J. Singh, and C. Fiolhais, *Phys. Rev. B* 48, 4978 (1993).
- [43] P. E. Blochl, *Phys. Rev. B* 50, 17953 (1994).
- [44] G. Kresse and D. Joubert, *Phys. Rev. B* 59, 1758 (1999).
- [45] Ashley P. Predith, Ph.D. thesis at MIT (2006).
- [46] J. Rosen, H. Park, J. Glick, and L. Zhang, *Comput. Optim. Appl.* 17, 329 (2000).
- [47] Anton Van der Ven, Ph.D. thesis at MIT (2000).
- [48] M. O. Zacate, L. Minervini, D. J. Bradfield, R. W. Grimes, and K. E. Sickafus, *Solid State Ionics* 128, 243 (2000).
- [49] P. Li, I. Chen, and J. E. Penner-Hahn, *Phys. Rev. B* 48, 10074 (1993)
- [50] P. Li and I. Chen, *J. Am. Ceram. Soc.* 77, 118 (1994).
- [51] C. R. A. Catlow, A. V. Chadwick, G. N. Greaves, and L. M. Moroney, *J. Am. Ceram. Soc.* 69, 272 (1986).
- [52] E. Lee, Wei Cai, and Friedrich B. Prinz, *Electrochemistry Communications* 12, 223 (2010)
- [53] J.E. Randles. Kinetics of rapid electrode reactions, *Discuss. Faraday Soc.* 1, 11 (1947).

- [54] S. Ikeda, O. Sakurai, K. Uematsu, N. Mizutani, and M. Kato, *J. Mater. Sci.* 20, 4593 (1985).
- [55] A. I. Ioffe, D. S. Rutman and S. V Karyachov, *Electrochim. Acta.* 23, 141 (1978).
- [56] D. W. Strickler and W. G. Carlson, *J. Am. Ceram. Soc.* 47, 122 (1964).
- [57] R. E. W. Casselton, *Phys. Stat. Sol. (a)* 2, 571 (1970).
- [58] J. D. Solier, I. Cachadna, and A. Dominguez-Rodriguez, *Phys. Rev. B.* 48, 3704 (1993).
- [59] Y. Chiang, D. Birnie III, and W. Kingery, *Physical Ceramics: The MIT series in Materials Science and Engineering*, Wiley (1997).
- [60] Y.R. Li, Z. Liang, Y. Zhang, J. Zhu, S.W. Jiang and X.H. Wei, *Thin Solid Films* 489, 245 (2005).
- [61] C.-h. Chiu, Z. Huang, and C. T. Poh, *Phys. Rev. Lett.* 93, 136105 (2004).
- [62] C. Bae, H. Shin, J. Moon and M.M. Sung, *Chem. Mater.* 18, 1085 (2006).